ACS Energy LETTERS

http://pubs.acs.org/journal/aelccp

Letter

Operando Time-of-Flight Secondary Ion Mass Spectrometry Visualization of Reversible and Irreversible Reactions in Oxide-Based Solid-State Batteries

Sihao Xing, Gen Hasegawa, Prince Sharma, Daisuke Ito, Kazuhiro Kamiguchi, Kazunori Takada, and Naoaki Kuwata*

Cite This: *ACS Energy Lett.* 2026, 11, 1889−1896

Read Online

ACCESS | Metrics & More | Article Recommendations | Supporting Information

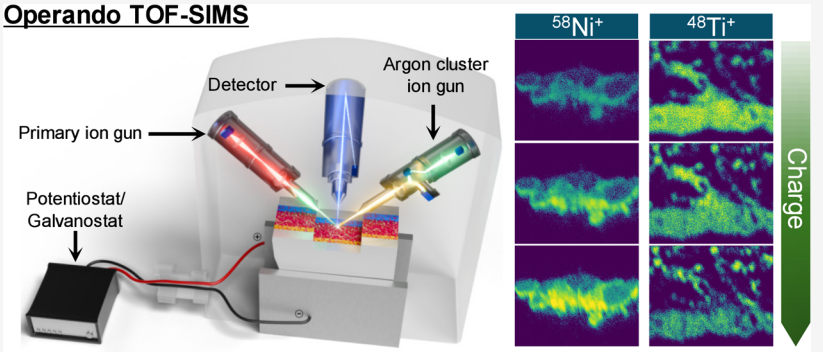

ABSTRACT: Operando time-of-flight secondary ion mass spectrometry (TOF-SIMS) was applied to solid-state batteries (SSBs) to visualize the dynamic electrode reactions. The SSBs consist of a $LiNi_{0.8}Co_{0.15}Al_{0.05}O_2$ (NCA) composite positive electrode, a $Li_4Ti_5O_{12}$ (LTO) composite negative electrode, and a $Li_2OHCl_{0.9}F_{0.1}/Li_{0.31}La_{0.56}TiO_3$ composite solid electrolyte, which were fabricated by a pressure-assisted melt infiltration method. Reversible changes in $^6Li^+$, $^{58}Ni^+$, and $^{48}Ti^+$ intensities were observed during charge−discharge processes. The intensity change of transition metal secondary ions is attributed to changes in ionization efficiency (matrix effects) and correlates with the state of charge. Reaction inhomogeneity was detected in the NCA composite electrode, indicating that the solid electrolyte infiltration has a positive effect on the electrochemical performance, whereas the LTO electrode exhibited uniform reaction distribution. These findings demonstrate that operando TOF-SIMS can provide critical insights into reaction distribution and irreversible capacity in SSBs, thereby guiding the optimization of electrode architectures.

Solid-state batteries (SSBs) that utilize solid electrolytes offer enhanced safety and energy density, positioning them as promising candidates for next-generation energy storage systems.[1−5] However, due to the entirely solid nature of SSBs, interface issues arise, such as loose contacts between particles and crack formation due to volume changes.[6−12] These interfacial issues hinder ion transport, leading to nonuniform electrochemical reactions within the electrodes, which in turn cause capacity loss.[13−16] To solve this problem, a technology must be developed that visualizes the diffusion of lithium ions. Despite its significance, few techniques are currently available for visualizing the spatial distribution of lithium ions, primarily due to the inherent difficulty of detecting lithium—with its low electron density—using conventional electron or X-ray-based methods. Recently, advanced methods for visualizing Li distribution have been reported using scanning transmission electron microscopy (STEM) with electron energy loss spectroscopy (EELS), which can visualize Li distribution in active materials at the nanometer scale.[17,18] However, this method has a limited observation range and usually detects only a few active material particles. Nuclear magnetic resonance (NMR) imaging[19,20] and X-ray photoelectron spectroscopy (XPS)[21,22] are also methods that can be used to investigate the spatial distribution of Li; however, they have limitations in terms of spatial resolution. Time-of-flight secondary ion mass spectrometry (TOF-SIMS) is a technique that allows for the study of lithium distribution with high spatial resolution and sensitivity by analyzing the mass of Li^+ ions.[23−39] Additionally, it can distinguish isotopes and measure other elements simultaneously. Its spatial resolution ranges from several nanometers to the micrometer range. Unlike STEM-EELS, it is well suited for wide-area analysis and can

Received: November 1, 2025
Revised: December 10, 2025
Accepted: January 5, 2026
Published: January 9, 2026

https://doi.org/10.1021/acsenergylett.5c03610
ACS Energy Lett. 2026, 11, 1889−1896

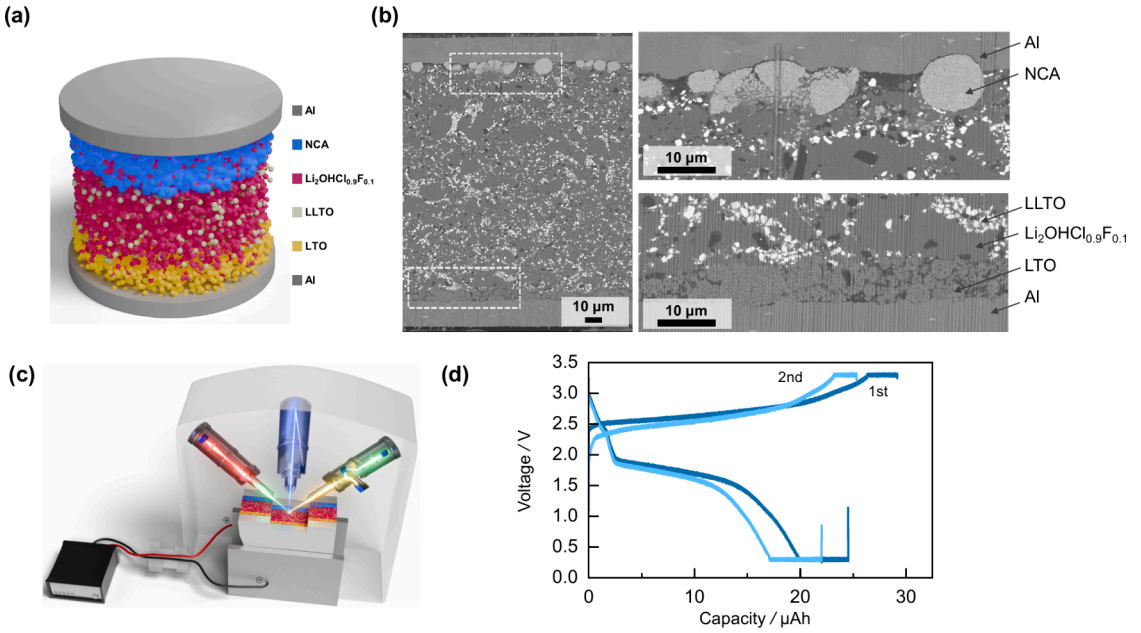

Figure 1. (a) Schematic of the solid-state battery. (b) Cross-sectional SEM image of the SSB. (c) Schematic of operando TOF-SIMS. (d) Charge−discharge curves of the first and second cycles of the SSB during operando TOF-SIMS measurements.

complement SEM by enabling, for instance, the simultaneous observation of both the positive and negative electrodes.

Applying TOF-SIMS to solid-state batteries enables operando observation of the charging and discharging processes. Masuda et al. initially reported that changes in the intensity of Li^+ in cathode active materials, $LiCoPO_4$, in an SSB can be visualized through operando TOF-SIMS.[37] They also noted that the apparent Li^+ intensity undergoes changes due to ion beam damage. Yamagishi et al. employed operando TOF-SIMS to visualize the process of Li extraction from the cathode active materials ($LiNi_{0.8}Co_{0.15}Al_{0.05}O_2$) and insertion into the anode active materials (graphite) in sulfide solid-state batteries.[23,38] As demonstrated by Walther et al., ex situ TOF-SIMS analysis of sulfide SSBs can detect reaction products at the cathode/electrolyte interface with high sensitivity and elucidate the degradation mechanism.[27] Bessette et al. studied the matrix effect of the cathode active material ($LiNi_{0.5}Mn_{0.3}Co_{0.2}O_2$) by ex situ TOF-SIMS analysis to provide a quantitative analysis of Li.[35] Previous operando TOF-SIMS studies have mainly focused on lithium species. However, their mobility under primary-ion bombardment hampers the direct visualization of charge−discharge reactions. In this work, we instead target transition-metal species ($^{58}Ni^+$ and $^{48}Ti^+$), which are immobile and less affected by primary-ion irradiation. We demonstrate that changes in their signal intensity can reasonably reflect the state of charge during cycling, enabling wide-field and reversible imaging of the reaction processes. Here, TOF-SIMS is positioned as a technique capable of simultaneously visualizing positive and negative electrodes in oxide-based solid-state batteries, offering new insights into reaction distributions and capacity loss.

The SSBs were prepared by a pressure-assisted melt infiltration method.[40] The battery fabrication details are documented in the Supporting Information and another paper[41] and will be briefly described here. The configuration of the solid-state battery is composed of five layers: Al current collector/composite anode/composite solid electrolyte/composite cathode/Al current collector. Figure 1(a) shows a schematic illustration of the SSB. The active materials for the negative and positive electrodes are $Li_4Ti_5O_{12}$ (LTO) and $LiNi_{0.8}Co_{0.15}Al_{0.05}O_2$ (NCA), respectively. The composite solid electrolyte is composed of perovskite-type $Li_{0.31}La_{0.56}TiO_3$ (LLTO) and antiperovskite-type $Li_2OHCl_{0.9}F_{0.1}$.[42−44] The combination of these solid electrolytes, which possess matched lattice constants, enables high ionic conductivity.[41] In this study, we employed a melt-infiltrated configuration as a model solid-state battery that can operate without external cell pressure during cycling, thereby enabling operando cross-sectional TOF-SIMS measurements. Although this configuration does not fully reproduce the external stack pressure or multilayer architecture of practical solid-state battery stacks, it captures the essential solid-electrolyte−active-material interfaces established through melt infiltration.

Figure 1(b) presents SEM images of the SSB cross section prior to operando SIMS. The specimen cross section was smoothed by focused ion beam (FIB) machining. The layers of Al, the cathode, the solid electrolyte, the anode, and Al are visible. The square regions depicted in the SEM image correspond to the areas observed in the operando SIMS, and they are shown magnified. In the composite cathode region, spherical NCA secondary particles are cracked and the solid electrolyte is observed to have soaked into the gaps by pressure-assisted melt-infiltration. Such cracking together with electrolyte penetration facilitated by melt-infiltration has been reported to stabilize interfacial resistance and enhance cycling performance.[41] In the region of the solid electrolyte, the presence of white LLTO particles, gray $Li_2OHCl_{0.9}F_{0.1}$, and black regions corresponding to LiOH is observed. In the anode region, spherical LTO particles possess a porous structure, with the $Li_2OHCl_{0.9}F_{0.1}$ electrolyte filling the gaps (Figure S1 in the Supporting Information).[41] This sample exhibits a high degree of density with minimal voids. Electrochemical and structural characterizations including electrochemical impedance spectroscopy, three-dimensional SEM, and STEM have been reported in our previous work.[41]

https://doi.org/10.1021/acsenergylett.5c03610
ACS Energy Lett. 2026, 11, 1889−1896

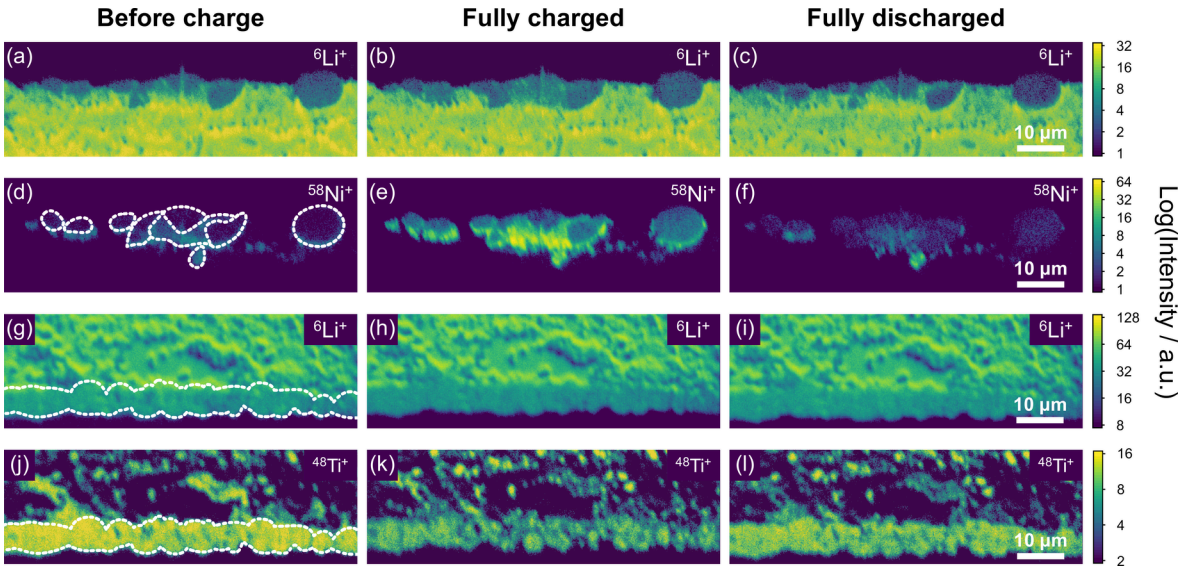

Figure 2. Secondary ion images obtained by operando TOF-SIMS. (a–c) $^{6}Li^{+}$ images of the positive electrode region: (a) before charging, (b) fully charged, and (c) fully discharged. (d–f) $^{58}Ni^{+}$ images of the positive electrode region. (g–i) $^{6}Li^{+}$ images of the negative electrode region. (j–l) $^{48}Ti^{+}$ images of the negative electrode region.

Figure 1(c) presents a schematic representation of the operando TOF-SIMS. The battery is positioned between two stainless steel plates and is connected to an electrochemical workstation, enabling operando measurements during charge and discharge cycling in the instrument (TOF.SIMS 5, IONTOF GmbH). TOF-SIMS enables wide-field visualization of reaction distributions in solid-state batteries and serves as a complementary technique to SEM. In this study, both the positive and negative electrode regions (each 80 × 30 μm^2) were captured simultaneously with a total integration time of 1600 s. The detailed measurement conditions are described in the Supporting Information.

Figure 1(d) shows the charge–discharge curves during operando TOF-SIMS measurements. The cathode and anode capacities of the SSB are designed to be 0.32 mAh cm^{-2} and 0.13 mAh cm^{-2}, respectively. This design enables the cathode to attain 40% utilization when the anode is fully charged. The area of each electrode is 0.2 cm^2. The constant current charge/discharge conditions are 0.03 mA cm^{-2} (0.2 C) and include a 1 h constant voltage hold. The charge capacity of the first cycle is 29 μAh (0.145 mAh cm^{-2}), which slightly exceeds the designed capacity of the negative electrode. The discharge capacity was 25 μAh (0.125 mAh cm^{-2}), showing an irreversible capacity of 14%. The charge and discharge capacities of the second cycle are 25 and 22 μAh, respectively. As will be shown later, this slight excess capacity may originate from side reactions involving the solid electrolyte (LLTO) on the anode side.

Figure 2 shows the operando TOF-SIMS results for the first cycle, with (a,f) representing the positive electrode region and (g,l) representing the negative electrode region. In the positive electrode, $^{6}Li^{+}$ and $^{58}Ni^{+}$ images are shown in (a)–(c) and (d)–(f), respectively, while in the negative electrode, $^{6}Li^{+}$ and $^{48}Ti^{+}$ images are shown in (g)–(i) and (j)–(l). Prior to imaging measurements, solid-state batteries were analyzed in TOF-SIMS spectrometry mode (Figure S2 in the Supporting Information), confirming that transition-metal ion signals (e.g., $^{58}Ni^{+}$ and $^{48}Ti^{+}$) dominate over lithium-related fragments, enabling reliable imaging and accurate ion identification.

The NCA particles in the positive electrodes are outlined by white dotted lines. Upon full charge, the $^{6}Li^{+}$ intensity in the NCA slightly decreases, while the $^{58}Ni^{+}$ intensity clearly increases. Upon full discharge, the $^{6}Li^{+}$ intensity recovers and $^{58}Ni^{+}$ intensity decreases. These reversible changes indicate that variations in the secondary ion intensities correspond to compositional changes caused by Li extraction and insertion in NCA. Some NCA particles retain a high intensity of $^{58}Ni^{+}$ even after full discharge, suggesting heterogeneity in the electrochemical reaction. The complete TOF-SIMS experimental data, including intermediate charge–discharge states, are presented in Figures S3–S8. A similar trend is observed for $^{59}Co^{+}$, as shown in Figure S6 of the Supporting Information. Bessette et al. performed ex situ SIMS experiments on NMC-532 and reported that Li extraction during charging decreases $^{7}Li^{+}$ intensity and increases $^{58}Ni^{+}$, $^{55}Mn^{+}$, and $^{59}Co^{+}$ intensities.[31] At full charge, Li intensity drops one-third, whereas Ni, Mn, and Co intensities increase approximately 10-fold. These trends are consistent with the experimental results.

Although TOF-SIMS is inherently destructive, measurements conducted within or below the *static SIMS* regime (~10^{13} ions cm^{-2}) are effectively nondestructive because removal is limited to less than one surface monolayer (~10^{15} atoms cm^{-2}).[45] In our experiments, the primary ion dose was 1.2 × 10^{14} cm^{-2}, slightly exceeding the static limit but remaining below the monolayer density, equivalent to the removal of approximately one monolayer over ten measurements. Thus, the operando conditions used here allow practical multicycle observation with minimal material loss, although irradiation-induced redistribution of mobile ions cannot be fully excluded.

The LTO particles in the negative electrodes are indicated by the white dotted line in Figure 2(g) and (j). The signal observed above the LTO particles in the ^{48}Ti map is attributed to the LLTO solid electrolyte particles. The Li concentration in the LTO increases with charging, while the $^{6}Li^{+}$ intensity displays a negligible change during the charging and discharging processes. The detailed reason the $^{6}Li^{+}$ intensity remains unchanged is unclear, but there are several reasons.

https://doi.org/10.1021/acsenergylett.5c03610
ACS Energy Lett. 2026, 11, 1889–1896

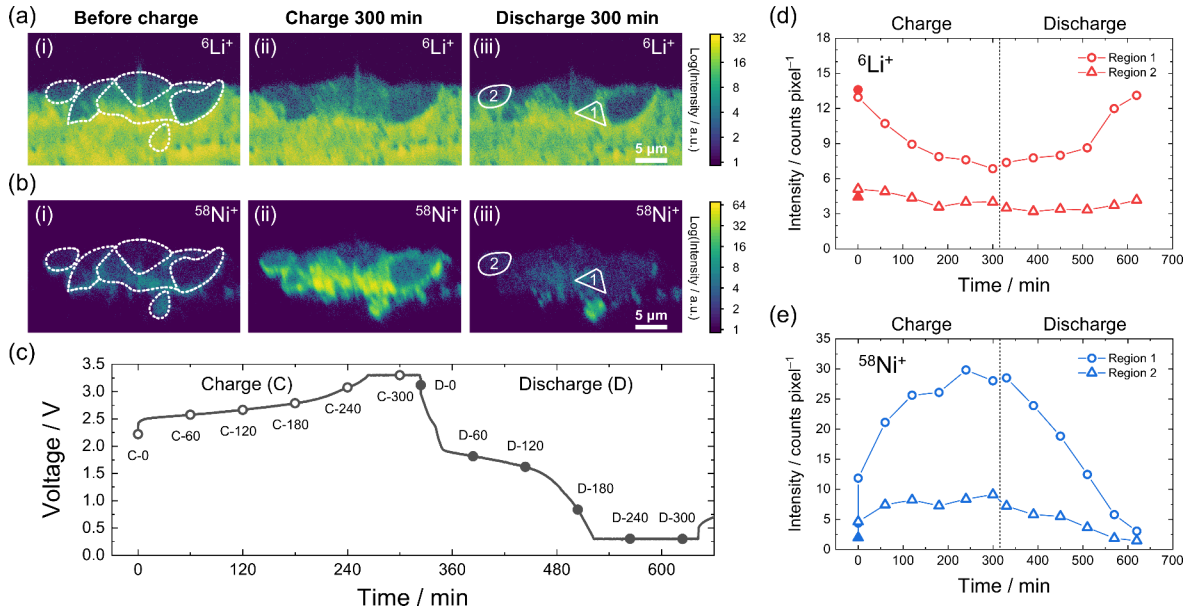

Figure 3. Enlarged images of (a) $^{6}Li^{+}$ and (b) $^{58}Ni^{+}$ ions in the positive electrode region obtained by operando TOF-SIMS. Images are shown for the status before charging, after the first charge, and after discharge. (c) Charge−discharge curve and TOF-SIMS observation points. Intensity changes per unit area in regions 1 and 2, indicated by the solid white lines, are for (d) $^{6}Li^{+}$ and (e) $^{58}Ni^{+}$.

One is that the LTO has a porous structure with a size of less than 200 nm and forms a dense composite with the electrolyte (Figure S1).[41] Therefore, with the SIMS spatial resolution (~2 μm), the electrolyte and anode signals overlap on the same pixel. The second is the influence of the matrix effect caused by changes in the chemical potential of LTO, which will be discussed later. Additionally, the diffusion of Li^{+} ions within the anode may induce surface compositional alterations due to the impact of the primary ions. Conversely, it has been demonstrated that the $^{48}Ti^{+}$ intensity decreases at full charge and increases at full discharge. Because $^{48}Ti^{+}$ ions are not present in the electrolyte and do not diffuse, a reversible change in SIMS intensity was observed.

The mechanisms responsible for the observed increase in $^{58}Ni^{+}$ and the decrease in $^{48}Ti^{+}$ associated with the charging of SSBs remain to be elucidated. The ensuing sections will address this issue in detail. The secondary ion yield in SIMS is generally determined by the product of the sputter yield of the chemical species m (Y_m), the ionization probability (α_m^{+}), and the concentration of m in the surface layer (θ_m):[45]

$$I = I_p Y_m \alpha_m^{+} \theta_m \eta \quad (1)$$

where I_p is the primary ion flux and η is the transmission of the analysis system, both of which remain constant during operando experiments. The surface layer concentrations (θ_m) of $^{58}Ni^{+}$ and $^{48}Ti^{+}$ are not expected to change significantly during operando experiments; therefore, the observed intensity changes are governed by Y_m and α^{+}. In most cases, over 99% of the sputtered yield is neutral, and the probability of a particle escaping as an ion depends on the electronic and chemical states of the surface (the matrix effect). Consequently, the ionization probability for a particular element can vary dramatically, for example, from a metal as compared to its oxide.[45]

One factor that changes with charging in NCA positive electrodes and LTO negative electrodes is the electrochemical potential of the active material. Upon charging, the electrochemical potential of Li in the positive electrode decreases, increasing its tendency to attract Li^{+} and electrons. As a result, Ni^{+} ions can be more readily formed when Ni atoms are sputtered into a vacuum, losing electrons to the matrix. Conversely, in the negative electrode, the electrochemical potential of Li is higher, enhancing the tendency to release Li^{+} and electrons, which can make Ti^{+} formation less likely. The sputter yield Y_m increases with decreasing surface binding energy,[35] which may also change with charging. The surface energies of NCA and LTO during charging remain to be elucidated and constitute a subject for future study. Based on these considerations, we conclude that the changes in the ionization probability due to the matrix effect are responsible for the observed intensity variations of $^{58}Ni^{+}$ and $^{48}Ti^{+}$.

The $^{6}Li^{+}$ signals are also influenced by matrix effects. Accordingly, the decrease in the $^{6}Li^{+}$ intensity observed during charging from Figure 2(a) to 2(b) likely reflects a combination of factors: Li depletion from the NCA positive electrode, enhancement due to matrix effects associated with changes in chemical potential, and a comparatively minor contribution from the infiltrated solid electrolyte. Similarly, the nearly constant $^{6}Li^{+}$ intensity on the negative electrode in Figure 2(g),(h) can be interpreted as the net result of Li insertion into the LTO negative electrode, matrix effects, and the influence of the solid electrolyte.

The interpretation of signal variations arising from matrix effects is qualitative, reflecting relative changes observed during operando cycling rather than quantitative compositional information. Future integration of SIMS with complementary techniques such as XPS and X-ray absorption spectroscopy is expected to clarify the relationship between the state of charge and SIMS intensity variations.

Figures 3(a) and 3(b) show enlarged images of the $^{6}Li^{+}$ and $^{58}Ni^{+}$ ions in the positive electrode during the first charge−discharge cycle. Figure 3(c) presents the charge−discharge curve with the TOF-SIMS measurement points indicated. Figures 3(d) and 3(e) show the changes in $^{6}Li^{+}$ and $^{58}Ni^{+}$ intensities in regions 1 and 2, enclosed by the white solid lines.

https://doi.org/10.1021/acsenergylett.5c03610
ACS Energy Lett. 2026, 11, 1889−1896

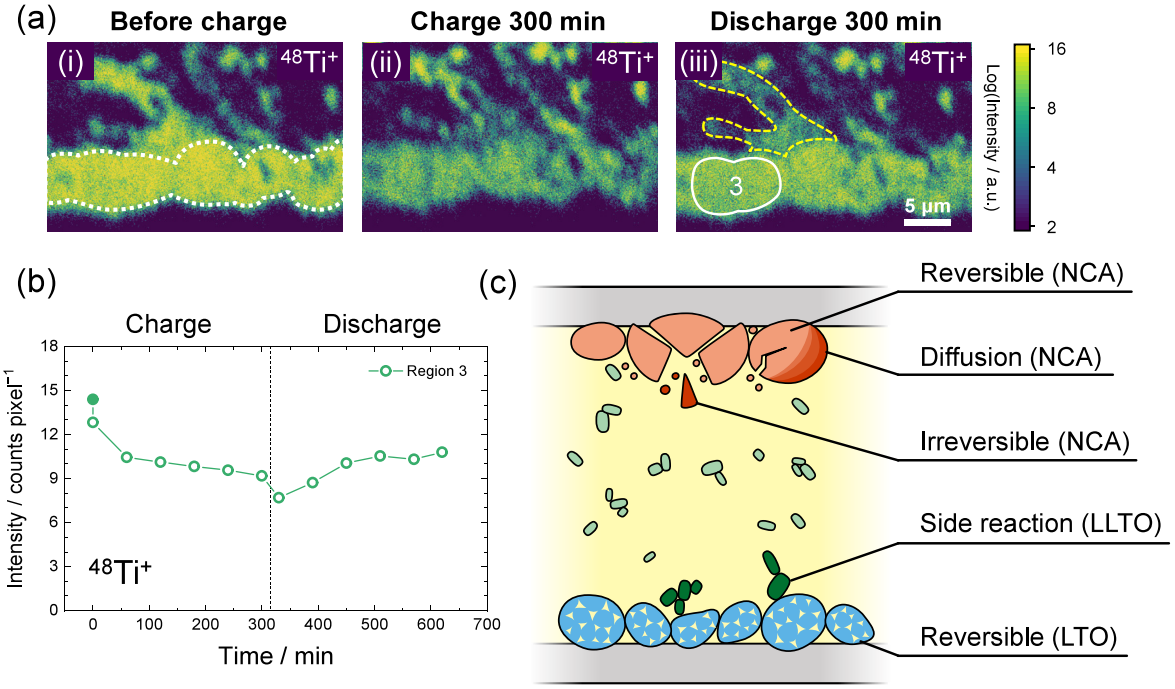

Figure 4. (a) Enlarged images of $^{48}Ti^{+}$ ions in the negative electrode region. These images show the states before charging, after full charge, and after full discharge. The area enclosed by the yellow dotted line corresponds to LLTO, which indicates an irreversible reaction. (b) Changes in the $^{48}Ti^{+}$ intensity in the region enclosed by the white line (region 3). (c) Schematic illustration of the reaction mechanisms revealed by operando TOF-SIMS.

For the second cycle, the charge−discharge curve and the corresponding TOF-SIMS images are provided in Figures S9−12 in the Supporting Information.

A magnified SEM image of the same region acquired prior to the operando measurements (Figure S1) shows that, in region 1, the NCA particles are fractured, and the solid electrolyte has penetrated the resulting gaps. This fracture and electrolyte infiltration occurred during sample preparation via the pressure-assisted infiltration method.[41] In contrast, the NCA particles in region 2 largely retained their original morphology. The changes in $^{6}Li^{+}$ and $^{58}Ni^{+}$ intensities are most pronounced in the fractured NCA particles in region 1, which can be interpreted because of shortened Li diffusion distances. As a result, the increase in $^{6}Li^{+}$ intensity during charging is inferred to be greater in region 1 than in region 2.

In region 2, the weaker intensity change indicates the reaction heterogeneity. These particles cycle reversibly but reach a state of charge shallower than those in region 1. Because the positive electrode capacity exceeds the negative electrode capacity, even small internal resistance differences may induce such heterogeneity. The inward increase in $^{58}Ni^{+}$ intensity suggests sluggish Li transport in region-2 secondary particles, likely due to limited diffusion across primary particle boundaries. In some NCA particles, the $^{58}Ni^{+}$ intensity remained strong, even after discharge, indicating an irreversible reaction. This heterogeneity is one of the factors contributing to irreversible capacity loss. As shown in Figure S16 of the Supporting Information, similar variations in $^{58}Ni^{+}$ intensity among individual NCA particles were observed in an additional sample, suggesting that this heterogeneous behavior is not an isolated effect but reasonably reflects electrode-level trends. Nonetheless, we note that TOF-SIMS is inherently surface-sensitive and does not directly probe bulk behavior; therefore, the conclusions derived from this technique should be interpreted within this analytical scope.

Figure 4(a) shows an enlarged view of the negative electrode region. The intensity of $^{48}Ti^{+}$ decreases during charging and increases with discharging, as shown in Figure 4(b). The LTO and the solid electrolyte form a nanoscale composite that enables more uniform electrochemical reactions compared with the positive electrode. A pronounced decrease in $^{48}Ti^{+}$ intensity was also observed in the solid electrolyte region adjacent to the negative electrode layer. As illustrated in Figure 4 (a), the intensity of the LLTO region (outlined by the yellow dotted line) decreases during charging and remains low even after discharge. The assignment of this region to LLTO was further supported by the Ti and La signals in the EDS data shown in the Supporting Information (Figure S15). Li insertion into LLTO around ∼1.5 V vs Li/Li^{+}, accompanied by Ti^{4+} reduction, has been reported in previous studies,[46−49] including those employing XPS analysis.[46,50] When electrons are supplied from the negative electrode, LLTO can be reduced with Li intercalation. We therefore interpret the observed low $^{48}Ti^{+}$ intensity to partial reduction of LLTO, which may contribute to irreversible capacity.

While LLTO enhances the ionic conductivity of composite solid electrolytes, it is preferable to employ it in configurations that avoid direct contact with the negative electrode. Figure 4(c) summarizes the reaction mechanisms revealed in this study. Irreversible capacity and Li diffusion were visualized in the NCA positive electrodes. In addition to reversible reactions at the negative electrode, part of the solid electrolytes was found to undergo reduction, contributing to irreversible capacity.

In summary, we applied operando TOF-SIMS technology to SSBs and demonstrated that transition metals ($^{58}Ni^{+}$, $^{48}Ti^{+}$) in the active material can be used to visualize reversible reactions.

https://doi.org/10.1021/acsenergylett.5c03610
ACS Energy Lett. 2026, 11, 1889−1896

We clarified that the intensity variations of transition-metal secondary ions arise from matrix effects associated with the charge−discharge state. It was observed that $Li_2OHCl_{0.9}F_{0.1}$ permeation enhances the electrochemical activity of the electrode materials. Furthermore, isolated NCA and electronically contacted LLTO were found to contribute to irreversible capacity. These insights highlight the potential of operando TOF-SIMS to facilitate the optimization of electrode architectures.

■ ASSOCIATED CONTENT

Supporting Information

The Supporting Information is available free of charge at https://pubs.acs.org/doi/10.1021/acsenergylett.5c03610.

Experimental details; SEM images of NCA and LTO particles (Figure S1); TOF-SIMS spectrometry mode (Figure S2); first cycle of operando TOF-SIMS (Figures S3−S8); second cycle of operando TOF-SIMS (Figures S9−S14); cross-sectional SEM-EDS (Figure S15); operando TOF-SIMS for an additional sample (Figure S16) (PDF)

■ AUTHOR INFORMATION

Corresponding Author

Naoaki Kuwata − *Center for Green Research on Energy and Environmental Materials, National Institute for Materials Science (NIMS), Tsukuba, Ibaraki 305-0044, Japan; Graduate School of Chemical Sciences and Engineering, Hokkaido University, Sapporo, Hokkaido 060-8628, Japan;* orcid.org/0000-0002-0736-6967; Email: KUWATA.Naoaki@nims.go.jp

Authors

Sihao Xing − *Center for Green Research on Energy and Environmental Materials, National Institute for Materials Science (NIMS), Tsukuba, Ibaraki 305-0044, Japan; Graduate School of Chemical Sciences and Engineering, Hokkaido University, Sapporo, Hokkaido 060-8628, Japan*

Gen Hasegawa − *Center for Green Research on Energy and Environmental Materials, National Institute for Materials Science (NIMS), Tsukuba, Ibaraki 305-0044, Japan;* orcid.org/0000-0002-9297-6902

Prince Sharma − *Center for Green Research on Energy and Environmental Materials, National Institute for Materials Science (NIMS), Tsukuba, Ibaraki 305-0044, Japan*

Daisuke Ito − *Corporate Technology & Business Development Unit, Murata Manufacturing Co., Ltd., Kyoto 617-8555, Japan;* orcid.org/0009-0006-9296-1926

Kazuhiro Kamiguchi − *Corporate Technology & Business Development Unit, Murata Manufacturing Co., Ltd., Kyoto 617-8555, Japan*

Kazunori Takada − *Center for Green Research on Energy and Environmental Materials, National Institute for Materials Science (NIMS), Tsukuba, Ibaraki 305-0044, Japan;* orcid.org/0000-0001-7568-1806

Complete contact information is available at: https://pubs.acs.org/10.1021/acsenergylett.5c03610

Notes

The authors declare no competing financial interest.

■ ACKNOWLEDGMENTS

This study was supported by NIMS All-Solid-State Battery Materials Open Platform (MOP) and the JST GteX Program, Grant Number JPMJGX23S2. This study was also supported by Materials Processing Science project ("Materealize") of MEXT, Grant Number JPMXP0219207397. This study was partly supported by JSPS KAKENHI, Grant Number 24H02205, "Ion Jamology". A part of this work was supported by the JST COI-NEXT program, Grant Number JPMJPF2016. The operando TOF-SIMS, FIB, SEM, and EDS measurements were supported by the NIMS technical support (NIMS Battery Research Platform).

■ REFERENCES

(1) Fan, L.; Wei, S.; Li, S.; Li, Q.; Lu, Y. Recent Progress of the Solid-State Electrolytes for High-Energy Metal-Based Batteries. *Adv. Energy Mater.* **2018**, *8* (11), No. 1702657.

(2) Xia, W.; Zhao, Y.; Zhao, F.; Adair, K.; Zhao, R.; Li, S.; Zou, R.; Zhao, Y.; Sun, X. Antiperovskite Electrolytes for Solid-State Batteries. *Chem. Rev.* **2022**, *122* (3), 3763−3819.

(3) Chen, J.; Wu, J.; Wang, X.; Zhou, A.; Yang, Z. Research Progress and Application Prospect of Solid-State Electrolytes in Commercial Lithium-Ion Power Batteries. *Energy Storage Mater.* **2021**, *35*, 70−87.

(4) Zheng, F.; Kotobuki, M.; Song, S.; Lai, M. O.; Lu, L. Review on Solid Electrolytes for All-Solid-State Lithium-Ion Batteries. *J. Power Sources.* **2018**, *389*, 198−213.

(5) Sun, C.; Liu, J.; Gong, Y.; Wilkinson, D. P.; Zhang, J. Recent Advances in All-Solid-State Rechargeable Lithium Batteries. *Nano Energy* **2017**, *33*, 363−386.

(6) Famprikis, T.; Canepa, P.; Dawson, J. A.; Islam, M. S.; Masquelier, C. Fundamentals of Inorganic Solid-State Electrolytes for Batteries. *Nat. Mater. 2019 18:12* **2019**, *18* (12), 1278−1291.

(7) Iriyama, Y. Preparation of Model Solid-State Batteries for Interface Ionics. In *Interface Ionics: For All-Solid-State Batteries and Solid State Ionics Devices*, Iriyama, Y.; Amezawa, K.; Tateyama, Y.; Yabuuchi, N., Eds.; The Materials Research Society Series; Springer: Singapore, 2024; pp 11−20.

(8) Amezawa, K.; Kimura, Y.; Nakamura, T. Basic Concept of Electrolyte Protection for Stable Operation of All-Solid-State Batteries—From the Perspective of Solid State Ionics. In *Interface Ionics: For All-Solid-State Batteries and Solid State Ionics Devices*, Iriyama, Y.; Amezawa, K.; Tateyama, Y.; Yabuuchi, N., Eds.; The Materials Research Society Series; Springer: Singapore, 2024; 163−173.

(9) Kuwata, N.; Hasegawa, G. Pulsed Field Gradient Nuclear Magnetic Resonance Measurement of Lithium Diffusion in Solid Electrolytes. In *Interface Ionics: For All-Solid-State Batteries and Solid State Ionics Devices*, Iriyama, Y.; Amezawa, K.; Tateyama, Y.; Yabuuchi, N., Eds.; The Materials Research Society Series; Springer: Singapore, 2024; pp 273−284.

(10) Kobayashi, S.; Nishio, K.; Wilde, M.; Fukutani, K.; Shimizu, R.; Hitosugi, T. Protons Inside the $LiCoO_2$ Electrode Largely Increase Electrolyte−Electrode Interface Resistance in All-Solid-State Li Batteries. *J. Phys. Chem. C* **2023**, *127* (9), 4684−4688.

(11) Yang, H.; Wu, N. Ionic Conductivity and Ion Transport Mechanisms of Solid-State Lithium-Ion Battery Electrolytes: A Review. *Energy Sci. Eng.* **2022**, *10* (5), 1643−1671.

(12) Xu, L.; Tang, S.; Cheng, Y.; Wang, K.; Liang, J.; Liu, C.; Cao, Y.-C.; Wei, F.; Mai, L. Interfaces in Solid-State Lithium Batteries. *Joule* **2018**, *2* (10), 1991−2015.

(13) Hasegawa, G.; Kuwata, N.; Ohnishi, T.; Takada, K. Visualization and Evaluation of Lithium Diffusion at Grain Boundaries in $Li_{0.29}La_{0.57}TiO_3$ Solid Electrolytes Using Secondary Ion Mass Spectrometry. *J. Mater. Chem. A* **2024**, *12* (2), 731−738.

(14) Tian, C.; Xu, Y.; Nordlund, D.; Lin, F.; Liu, J.; Sun, Z.; Liu, Y.; Doeff, M. Charge Heterogeneity and Surface Chemistry in Polycrystalline Cathode Materials. *Joule* **2018**, *2* (3), 464−477.

(15) Naik, K. G.; Vishnugopi, B. S.; Mukherjee, P. P. Heterogeneities Affect Solid-State Battery Cathode Dynamics. *Energy Storage Mater.* **2023**, *55*, 312−321.
(16) Vishnugopi, B. S.; Kazyak, E.; Lewis, J. A.; Nanda, J.; McDowell, M. T.; Dasgupta, N. P.; Mukherjee, P. P. Challenges and Opportunities for Fast Charging of Solid-State Lithium Metal Batteries. *ACS Energy Lett.* **2021**, *6* (10), 3734−3749.
(17) Nomura, Y.; Yamamoto, K.; Hirayama, T.; Ohkawa, M.; Igaki, E.; Hojo, N.; Saitoh, K. Quantitative Operando Visualization of Electrochemical Reactions and Li Ions in All-Solid-State Batteries by STEM-EELS with Hyperspectral Image Analyses. *Nano Lett.* **2018**, *18* (9), 5892−5898.
(18) Nomura, Y.; Yamamoto, K.; Kuwata, N.; Hirayama, T. Imaging Phase Boundary Kinetics in Lithium Titanate Using Operando Electron Energy-Loss Spectroscopy. *ACS Energy Lett.* **2025**, *10*, 1404−1410.
(19) Chandrashekar, S.; Trease, N. M.; Chang, H. J.; Du, L. S.; Grey, C. P.; Jerschow, A. ^{7}Li MRI of Li Batteries Reveals Location of Microstructural Lithium. *Nat. Mater.* **2012**, *11* (4), 311−315.
(20) Hellar, N.; Iwai, Y.; Ohzu, M.; Brox, S.; Dorai, A.; Takekawa, R.; Kuwata, N.; Kawamura, J.; Winter, M. Direct Observation of Mn-Ion Dissolution from $LiMn_2O_4$ Lithium Battery Cathode to Electrolyte. *Commun. Mater.* **2025**, *6* (1), 23.
(21) Endo, R.; Ohnishi, T.; Takada, K.; Masuda, T. In Situ Observation of Lithiation and Delithiation Reactions of a Silicon Thin Film Electrode for All-Solid-State Lithium-Ion Batteries by X-Ray Photoelectron Spectroscopy. *J. Phys. Chem. Lett.* **2020**, *11* (16), 6649−6654.
(22) Endo, R.; Ohnishi, T.; Takada, K.; Masuda, T. Electrochemical Lithiation and Delithiation in Amorphous Si Thin Film Electrodes Studied by Operando X-Ray Photoelectron Spectroscopy. *J. Phys. Chem. Lett.* **2022**, *13* (31), 7363−7370.
(23) Yamagishi, Y.; Morita, H.; Nomura, Y.; Igaki, E. Visualizing Lithiation of Graphite Composite Anodes in All-Solid-State Batteries Using Operando Time-of-Flight Secondary Ion Mass Spectrometry. *J. Phys. Chem. Lett.* **2021**, *12* (19), 4623−4627.
(24) Priebe, A.; Aribia, A.; Sastre, J.; Romanyuk, Y. E.; Michler, J. 3D High-Resolution Chemical Characterization of Sputtered Li-Rich NMC811 Thin Films Using TOF-SIMS. *Anal. Chem.* **2022**, *95* (2), 1074−1084.
(25) Hasegawa, G.; Kuwata, N.; Tanaka, Y.; Miyazaki, T.; Ishigaki, N.; Takada, K.; Kawamura, J. Tracer Diffusion Coefficients of Li^+ ions Inc-Axis Oriented Li_xCoO_2 thin Films Measured by Secondary Ion Mass Spectrometry. *Phys. Chem. Chem. Phys.* **2021**, *23* (3), 2438−2448.
(26) Schwab, C.; Höweling, A.; Windmüller, A.; Gonzalez-Julian, J.; Möller, S.; Binder, J. R.; Uhlenbruck, S.; Guillon, O.; Martin, M. Bulk and Grain Boundary Li-Diffusion in Dense $LiMn_2O_4$ Pellets by Means of Isotope Exchange and ToF-SIMS Analysis. *Phys. Chem. Chem. Phys.* **2019**, *21* (47), 26066−26076.
(27) Walther, F.; Koerver, R.; Fuchs, T.; Ohno, S.; Sann, J.; Rohnke, M.; Zeier, W. G.; Janek, J. Visualization of the Interfacial Decomposition of Composite Cathodes in Argyrodite-Based All-Solid-State Batteries Using Time-of-Flight Secondary-Ion Mass Spectrometry. *Chem. Mater.* **2019**, *31* (10), 3745−3755.
(28) Morino, Y. Degradation Rate at the Solid−Solid Interface of Sulfide-Based Solid Electrolyte−Cathode Active Material. *J. Power Sources* **2022**, *541*, 231672.
(29) Zhou, Y.; Su, M.; Yu, X.; Zhang, Y.; Wang, J. G.; Ren, X.; Cao, R.; Xu, W.; Baer, D. R.; Du, Y.; Borodin, O.; Wang, Y.; Wang, X. L.; Xu, K.; Xu, Z.; Wang, C.; Zhu, Z. Real-Time Mass Spectrometric Characterization of the Solid−Electrolyte Interphase of a Lithium-Ion Battery. *Nat. Nanotechnol.* **2020**, *15* (3), 224−230.
(30) Brugge, R. H.; Chater, R. J.; Kilner, J. A.; Aguadero, A. Experimental Determination of Li Diffusivity in LLZO Using Isotopic Exchange and FIB-SIMS. *J. Phys. Energy* **2021**, *3* (3), 034001.
(31) Kuwata, N.; Lu, X.; Miyazaki, T.; Iwai, Y.; Tanabe, T.; Kawamura, J. Lithium Diffusion Coefficient in Amorphous Lithium Phosphate Thin Films Measured by Secondary Ion Mass Spectroscopy with Isotope Exchange Methods. *Solid State Ion.* **2016**, *294*, 59−66.
(32) Kuwata, N.; Hasegawa, G.; Maeda, D.; Ishigaki, N.; Miyazaki, T.; Kawamura, J. Tracer Diffusion Coefficients of Li Ions in $Li_xMn_2O_4$ Thin Films Observed by Isotope Exchange Secondary Ion Mass Spectrometry. *J. Phys. Chem. C* **2020**, *124* (42), 22981−22992.
(33) Kuwata, N.; Nakane, M.; Miyazaki, T.; Mitsuishi, K.; Kawamura, J. Lithium Diffusion Coefficient in $LiMn_2O_4$ Thin Films Measured by Secondary Ion Mass Spectrometry with Ion-Exchange Method. *Solid State Ion.* **2018**, *320*, 266−271.
(34) Dellen, C.; Gehrke, H. G.; Möller, S.; Tsai, C. L.; Breuer, U.; Uhlenbruck, S.; Guillon, O.; Finsterbusch, M.; Bram, M. Time-of-Flight Secondary Ion Mass Spectrometry Study of Lithium Intercalation Process in $LiCoO_2$ Thin Film. *J. Power Sources.* **2016**, *321*, 241−247.
(35) Bessette, S.; Paolella, A.; Kim, C.; Zhu, W.; Hovington, P.; Gauvin, R.; Zaghib, K. Nanoscale Lithium Quantification in $Li_xNi_yCo_wMnZO_2$ as Cathode for Rechargeable Batteries. *Sci. Rep.* **2018**, *8* (1), 1−9.
(36) Sui, T.; Song, B.; Dluhos, J.; Lu, L.; Korsunsky, A. M. Nanoscale Chemical Mapping of Li-Ion Battery Cathode Material by FIB-SEM and TOF-SIMS Multi-Modal Microscopy. *Nano Energy.* **2015**, *17*, 254−260.
(37) Masuda, H.; Ishida, N.; Ogata, Y.; Ito, D.; Fujita, D. In Situ Visualization of Li Concentration in All-Solid-State Lithium Ion Batteries Using Time-of-Flight Secondary Ion Mass Spectrometry. *J. Power Sources.* **2018**, *400*, 527−532.
(38) Yamagishi, Y.; Morita, H.; Nomura, Y.; Igaki, E. Visualizing Lithium Distribution and Degradation of Composite Electrodes in Sulfide-Based All-Solid-State Batteries Using Operando Time-of-Flight Secondary Ion Mass Spectrometry. *ACS Appl. Mater. Interfaces.* **2021**, *13* (1), 580−586.
(39) Tripathi, A. M.; Su, W. N.; Hwang, B. J. In Situ Analytical Techniques for Battery Interface Analysis. *Chem. Soc. Rev.* **2018**, *47* (3), 736−851.
(40) Xiao, Y.; Turcheniuk, K.; Narla, A.; Song, A.-Y.; Ren, X.; Magasinski, A.; Jain, A.; Huang, S.; Lee, H.; Yushin, G. Electrolyte Melt Infiltration for Scalable Manufacturing of Inorganic All-Solid-State Lithium-Ion Batteries. *Nat. Mater.* **2021**, *20* (7), 984−990.
(41) Ito, D.; Kuwata, N.; Takemoto, S.; Kamiguchi, K.; Hasegawa, G.; Takada, K. Lattice-matched antiperovskite-perovskite system toward all-solid-state batteries. *Nat. Commun.* **2025**, *16*, 7372.
(42) Hasegawa, G.; Kuwata, N.; Hashi, K.; Tanaka, Y.; Takada, K. Lithium-Ion Diffusion in Perovskite-Type Solid Electrolyte Lithium Lanthanum Titanate Revealed by Pulsed-Field Gradient Nuclear Magnetic Resonance. *Chem. Mater.* **2023**, *35* (10), 3815−3824.
(43) Song, A. Y.; Turcheniuk, K.; Leisen, J.; Xiao, Y.; Meda, L.; Borodin, O.; Yushin, G. Understanding Li-Ion Dynamics in Lithium Hydroxychloride (Li_2OHCl) Solid State Electrolyte via Addressing the Role of Protons. *Adv. Energy Mater.* **2020**, *10*, No. 1903480.
(44) Wang, F.; Evans, H. A.; Kim, K.; Yin, L.; Li, Y.; Tsai, P.-C.; Liu, J.; Lapidus, S. H.; Brown, C. M.; Siegel, D. J.; Chiang, Y.-M. Dynamics of Hydroxyl Anions Promotes Lithium Ion Conduction in Antiperovskite Li_2OHCl. *Chem. Mater.* **2020**, *32* (19), 8481−8491.
(45) Vickerman, J. C.; Briggs, D. *TOF-SIMS: Materials Analysis by Mass Spectrometry*, 2nd ed.; IM Publications: Chichester, West Sussex, 2013; pp 1−40.
(46) Zhang, L.; Zhang, X.; Tian, G.; Zhang, Q.; Knapp, M.; Ehrenberg, H.; Chen, G.; Shen, Z.; Yang, G.; Gu, L.; Du, F. Lithium Lanthanum Titanate Perovskite as an Anode for Lithium Ion Batteries. *Nat. Commun.* **2020**, *11* (1), DOI: 10.1038/s41467-020-17233-1.
(47) Klingler, M.; Chu, W. F.; Weppner, W. Coulometric titration of substituted $Li_xLa_{(2-x)/3}$ TiO_3. *Ionics* **1997**, *3* (3), 289−291.
(48) Ring, J.; Laa, L.; Limbeck, A.; Vonk, V.; Volkov, S.; Nenning, A.; Fleig, J. Electrochemical Stability Window and Electrolyte Breakdown Mechanisms of Lithium Lanthanum Titanate. *J. Electrochem. Soc.* **2023**, *170* (6), No. 060509.

https://doi.org/10.1021/acsenergylett.5c03610
ACS Energy Lett. 2026, 11, 1889−1896

(49) Takeno, S.; Watanabe, K.; Suematsu, K.; Shimanoe, K. Thickly and densely sintered $Li_{3x}La_{2/3-x}TiO_3$ electrodes for the anode of Li-ion batteries. *J. Ceram. Soc. Jpn.* **2025**, *133* (3), 80−85.
(50) Wenzel, S.; Leichtweiss, T.; Krüger, D.; Sann, J.; Janek, J. Interphase formation on lithium solid electrolytes—An in situ approach to study interfacial reactions by photoelectron spectroscopy. *Solid State Ionics* **2015**, *278*, 98−105.

https://doi.org/10.1021/acsenergylett.5c03610
ACS Energy Lett. 2026, 11, 1889−1896